ELECTRIMACS 2026 – Palermo, Italy, 18-21 May 2026

Verification of Stability Boundaries of Grid Following and Grid Forming Inverters through Real-Time Simulations

Yadala Pavan Kumar · Xi Luo · Efstratios Batzelis · Abhinav Kumar Singh · Georgia Saridaki · Panos Kotsampopoulos · Nikos Hatziargyriou

Abstract Inverter-based resources (IBRs) operate in either grid-following (GFL) or grid-forming (GFM) mode, with GFL acting as a current source prone to instability in weak grids and GFM functioning like a voltage source that struggles in very strong grids. The stability boundaries of both GFL and GFM vary with changes in key control and grid parameters, and offline simulation results are commonly validated using real-time simulation (RTS) platforms. This work explores for the first time how the stability boundaries in GFL and GFM differ in the two platforms (MATLAB /Simulink and Typhoon/RTS), highlighting the discrepancies between simulation results and practical real-time behaviour due to inherent complexities and non-ideal component characteristics. In addition, a modelling framework is introduced to translate the results of one platform to the other.

1 Introduction

The transition towards low-carbon energy systems is driving the adoption of more renewable-based power generation, such as solar photovoltaic, wind, fuel cells, and battery energy storage systems. These resources are integrated into the power system mostly via power electronic converters [1]. Conventional power systems are dominated by synchronous generators, which have well-established dynamic models and physical masses; in contrast, inverter-based resources (IBRs) depend on control-based mechanisms to interface with the grid. Their synchronisation behaviour and grid connection depend on control mechanisms rather than mechanical dynamics [2]. The control algorithms offer a fast response and high flexibility, but they also bring new challenges to system stability and control interactions. Based on how they interact with the grid and their control strategies, IBRs usually run in either grid-following (GFL) or grid-forming (GFM) mode [3].

GFL acts as a current source, regulates the AC-side current, and synchronises with the grid using the phase-locked loop (PLL). On the other hand, GFM serves as a voltage source, establishes its own voltage and frequency reference, and synchronises with the grid through mechanisms like frequency droop control. Both GFL and GFM have their own advantages and limitations. GFL performs well under strong grid conditions but exhibits poor performance in weak grids due to PLL susceptibility at volatile voltage [3]. In contrast, GFM provides a better dynamic response under weak conditions but struggles to maintain stability in very strong grids [4]. In recent years, several studies have focused on advancing inverter control strategies to address these limitations. Significant efforts have been made to improve GFM control techniques through enhanced voltage regulation, refined droop control strategies, and data-driven modelling, resulting in improved dynamic response [5–7]. Other studies have proposed adaptive or switching methods between GFL/GFM to improve stability over a wide range of short-circuit ratios (SCRs) [8,9]. Furthermore, hybrid control algorithms based on sequence impedance models and model predictive control (MPC) have been also introduced to operate the IBR reliably across a wide range of grid conditions [10,11].

On the other hand, several researchers have investigated how variations in control parameters affect the dynamic re-

---

Yadala Pavan Kumar · Xi Luo · Efstratios Batzelis · Abhinav Kumar Singh
School of Electronics and Computer Science
University of Southampton
High field campus, SO17 1BJ, Southampton, United Kingdom.
e-mail: pavankumaryadala008@gmail.com, xi.luo@soton.ac.uk, e.batzelis@soton.ac.uk, a.k.singh@soton.ac.uk

Georgia Saridaki · Panos Kotsampopoulos · Nikos Hatziargyriou
School of Electrical and Computer Engineering
National Technical University of Athens
Heroon Polytechniou 9, 15780 Zografou, Greece
e-mail: gsaridaki@power.ece.ntua.gr, kotsa@power.ece.ntua.gr, nh@power.ece.ntua.gr

Table 1: Comparative assessment of inverter studies

Ref	**GFL and GFM**	**Simulations**	**RTS validation**	**Simulation and RTS comparison**	**RTS stability boundary analysis**
[2],[3],[8],[10],[11]	✓	✓	✓	-	-
[4],[7]	GFM	-	✓	-	-
[5]	GFM	✓	✓	-	-
[6],[9],[12]	✓	✓	-	-	-
[14],[15]	GFL	✓	✓	✓	-
Proposed	✓	✓	✓	✓	✓

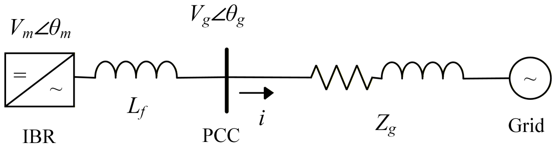

Fig. 1: Grid-connected inverter-based resource model.

sponse and stability boundaries of both GFM and GFL inverters. For example, Luo et al [12] examined the influence of key parameters, such as controller gains, active and reactive power references, droop coefficients, and filter cutoff frequencies, on the stability boundaries of GFL and GFM inverters using a boundary-tracking algorithm, thereby providing insights into parameter-dependent stability characteristics. In addition to theoretical and offline simulations, the authors in [3, 13] have highlighted the necessity of validating inverter models through RTS and significant practical challenges such as synchronisation issues and implementation constraints. Notably, the study in [14] compared the dynamic responses from pure digital and real-time simulations, observing substantial discrepancies between the two and Ref [15] takes the analysis further and compares the dynamic response with multiple RTS platforms. These results suggest that stability boundaries and dynamic responses predicted by theoretical models or offline simulations may not accurately represent behaviour observed in RTS settings. Therefore, platform-dependent effects resulting from non-ideal component behaviour and practical implementation constraints can alter stability boundaries representation and potentially impact overall system stability assessment. Given this context, differences between pure simulation studies and RTS platforms can result in deviations in stability margins. Consequently, validating these margins through RTS is essential for accurate and reliable performance assessment. The existing literature [2–12, 14] either uses simulation studies or RTS to validate their hypothesis, but does not explicitly compare the dynamic response or stability boundaries of the same model in both platforms, as highlighted in Table 1. Among all relevant papers, only [14, 15] performs a comparison between the two settings, but stays in time-domain response and does not expand to the much needed stability boundary.

In light of this gap, this paper performs a comprehensive comparison of stability representation for both GFL and GFM in the two platforms. The main contributions are:

- Investigating how the stability boundaries in GFL and GFM differ in the two platforms.
- Understanding the mechanism for these deviations and introducing a modelling framework to translate the results of one platform to the other.

2 Modeling

2.1 System configuration and IBR control architecture

In this study, an IBR connected to the infinite bus is considered, as shown in Fig.1. The IBR is connected to the grid through a filter (L_f) and grid impedance (Z_g).The IBR can be operated either in GFL or GFM mode. Both GFL and GFM have the same inner current controller, but separate outer loops to generate the phase angle (θ) and current references for the inner current control. In GFL mode, the PLL extracts the grid voltage angle (θ) and synchronises to the grid as shown in Fig.2(a), supported by $P(\omega)$ droop for primary frequency response. In GFM mode, standard droop control $(\omega(P))$ is used for both frequency response and grid synchronisation as shown in Fig.2(b). To generate the current references for GFL and GFM, separate outer loops are used as shown in Fig.2(c) and Fig.2(d).

The circuit of Fig.1 and control schemes of Fig.2 are implemented in both simulations (MATLAB/Simulink) and RTS (Typhoon) environments. During the implementation of the models in RTS, to avoid practical implementation issues (overrun flags), additional saturation blocks included as highlighted in red in Fig.2.

2.2 Stability boundary extraction for GFL and GFM

Stability boundary refers to the set of parameters that drive the system marginally stable. Depending on the number of parameters of interest (e.g. SCR, power set points, control parameters), it can have multiple dimensions [12]; however, in practice we employ 2-dimensional boundaries that are readily visualised, most often SCR vs another parameter of interest.The theoretical stability boundaries of GFL and GFM can be obtained in 2-dimensional search as discussed in [12]. This work is an extension of [12] and focuses on experimental identification of stability boundaries. The 2-dimensional boundary, or curve, can be obtained with the parameter of interest (X_i) and SCR, where (X_i) can be any grid or con-

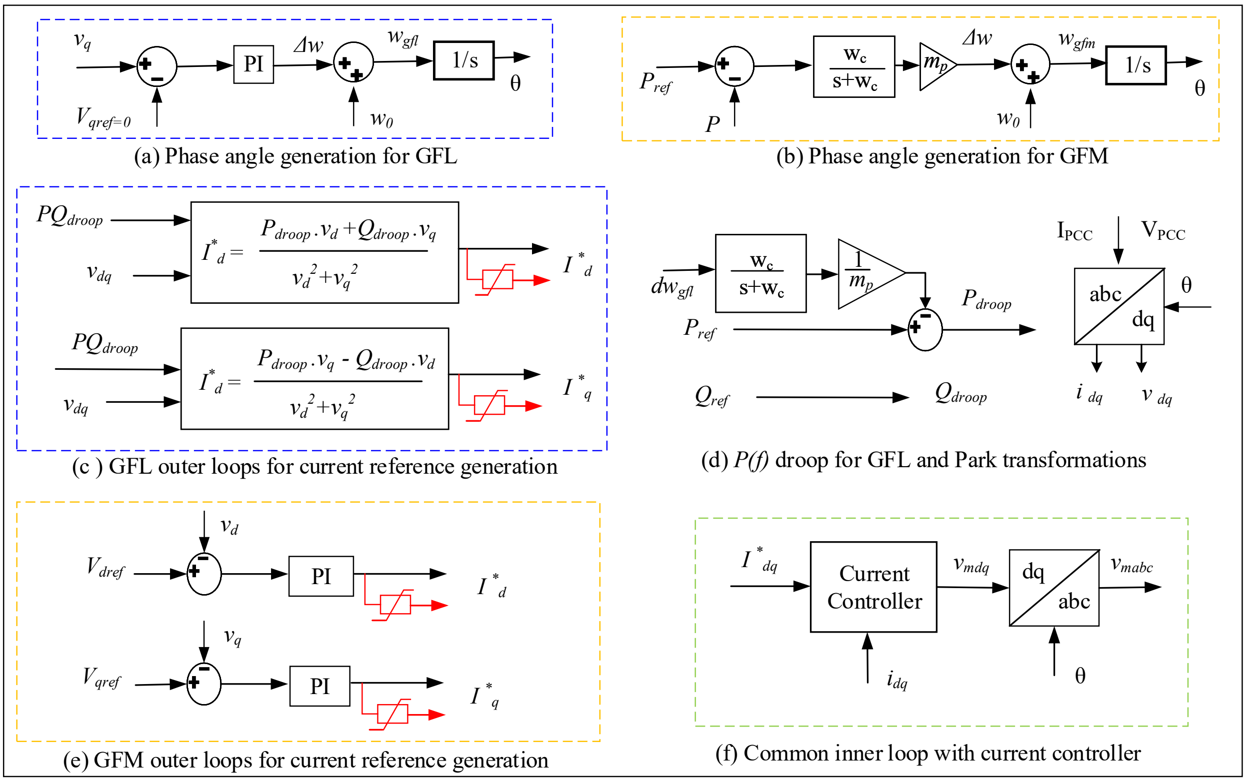

Fig. 2: GFL and GFM control architecture.

trol parameter, most often the droop coefficient (mp) or the power set points (P_{ref}, Q_{ref}).

The flowchart of experimental identification of X_i - SCR stability curve via either simulations or RTS is given in Fig.4. For a particular value of X_i, the model will be executed repeatedly between the SCR_{min} and SCR_{max} to get the critical stability boundary (SCR_{crt}). Once SCR_{crt} is obtained for X_i, the process is repeated for additional X_i values until X_i^{max}. The points (X_i, SCR_{crt}) identified represent the stability curve, which can be visualised via plots and characterise the stable and unstable regions. For example, the stability curves $(mp$ vs $SCR)$ in RTS for GFL and GFM are shown in Fig.3. The SCR can be calculated as given in Eq.1 for the Thevenin's equivalent model given in Fig.1. In Fig.4, ΔSCR is set to 0.05 and ΔX is chosen empirically depending on the parameter (X_i).

$$\text{SCR} = \frac{P_{\text{sc}}}{P_n} = \frac{|V_{rated}|^2}{|Z_g|\,P_n} \tag{1}$$

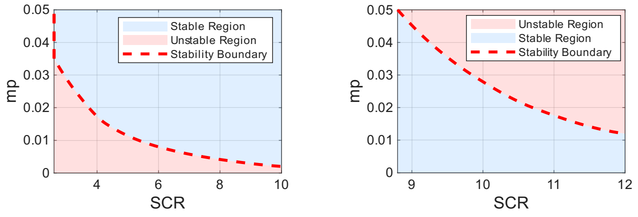

(a) GFL (b) GFM

Fig. 3: Illustration of 2-dimensional Stability boundaries.

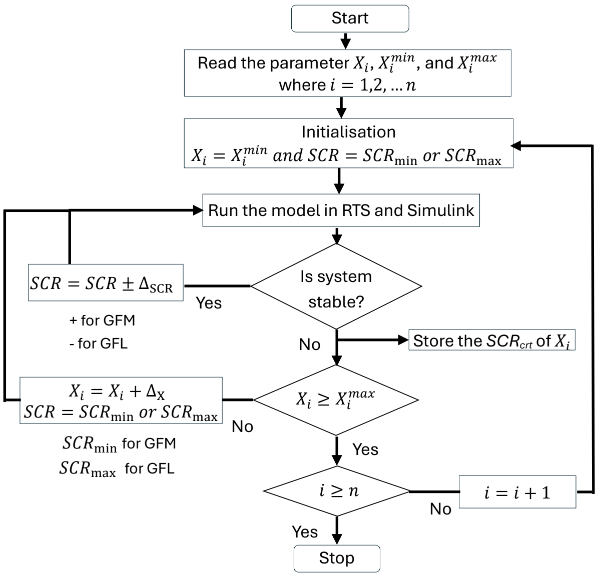

Fig. 4: Stability boundary extraction for GFL and GFM in RTS and Simulink.

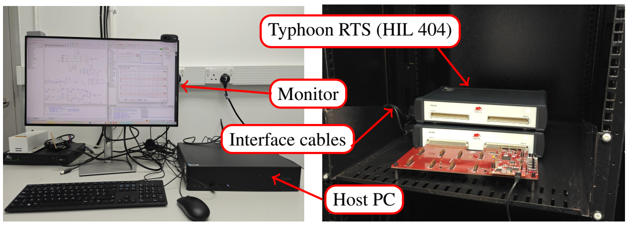

Fig. 5: Typhoon RTS setup.

Table 2: Test System Parameters

S. No	Parameter	Value
1	Base power	10 MVA
2	System frequency (f_0)	50 Hz
3	IBR active power set point (P_{ref})	1 p.u.
4	IBR reactive power set point (Q_{ref})	0 p.u.
5	PLL proportional gain (k_p)	1.4
6	PLL integral gain (k_i)	5000
7	Droop coefficient (m_p)	1 % and 5 %
9	Current controller proportional gain (k_{pi})	1.25
10	Current controller integral gain (k_{ii})	10
11	Low-pass filter cutoff frequency (f_c)	10 Hz and 20 Hz
12	Voltage controller proportional gain (k_{pv})	5
13	Voltage controller integral gain (k_{iv})	250

3 Results

The test system considered in Fig.1 has been simulated in both Simulink and the Typhoon RTS setup shown in Fig.5. The parameters considered in this study are given in Table 2. The droop coefficient mp is set to 1% in GFL and 5% in GFM, while the LPF cut-off frequency (f_c) is set to 10 Hz in GFL and 20 Hz in GFM. In RTS, the Euler method has been used for discretisation, with a solver execution time step of 0.2μs and a signal processing time step of 4μs. Initially, the dynamic response in the two platforms is analysed to highlight discrepancies, and later the stability boundaries are extracted across both platforms using the methodology described in section 2.2.

3.1 Dynamic response analysis

The GFL and GFM models with the same parameters are simulated in RTS and Simulink to compare the dynamic response across the platforms. The active power (P) of the IBR have been sampled at 1 μs time step, and a 10% change in active power setpoint is applied at 3s to trigger system dynamics. It is noteworthy that in RTS the solver and signal processing execution time steps are kept as small as possible given the hardware constraints. For GFL, the active power response is given at different grid strengths in Fig.6. At strong grid conditions (ex.SCR 6), the dynamic response from RTS and Simulink are aligned, but as the grid strength reduces (ex.SCR 5), the response starts to deviate. Ultimately, at SCR 3.3, the model in RTS becomes unstable, but the model in Simulink is stable with positive damping. When it comes to GFM, the same analysis has been carried out and it is observed that under relatively weak grid conditions (ex.SCR 4) the dynamic response from both platforms align well. However, deviations between the two platforms are observed at stronger grid, with Simulink becoming unstable at SCR 7 when RTS exhibits still positive damping. It is worth highlighting the opposite trend in the two platforms mismatch for GFL and GFM: the discrepancy is higher in weak grids for GFL, but in strong grids for GFM.

3.2 Stability boundary analysis

More insight on this divergence can be obtained via the stability curves. The 2-dimensional stability boundaries for the parameters m_p, P_{ref}, and Q_{ref} vs SCR are obtained for both GFL and GFM as shown in Fig.8 and Fig.9. A quick glance reveals that the curves from the two platforms have the same shape, but exhibit a horizontal shift of a certain SCR offset. It is interesting to see that the RTS stability curve (red) lies consistently on the right side of the Simulink curve (blue) in both GFL and GFM results, which suggests an underlying mismatch mechanism yet to be revealed.

This systematic shift can be attributed to additional dynamics inherently introduced by the RTS platform, such as numerical solvers, fixed-step discretisation, computational and synchronisation delays [16]. While these delays do not correspond to a physical element, their aggregated effect modifies the dynamic interaction between the inverter and the grid. From a system-level perspective, this influence can be equivalently represented by an additional effective impedance term, *delay impedance (Z_d)*, which augments the nominal grid impedance Z_g. Therefore, the effective grid impedance seen by the inverter in RTS can be expressed as

$$Z_{\text{eff}} = Z_g + Z_d \tag{2}$$

Accordingly, the effective short-circuit ratio experienced by the inverter becomes

$$\text{SCR}_{\text{eff}} = \frac{V_{\text{rated}}^2}{P_{\text{n}}|Z_{\text{eff}}|} = \frac{V_{\text{rated}}^2}{P_{\text{n}}|Z_g + Z_{\text{d}}|} < \frac{V_{\text{rated}}^2}{P_{\text{n}}|Z_g|} = \text{SCR}_{\text{g}} \tag{3}$$

This relationship implies that, the RTS outputs correspond to a weaker grid (SCR_{eff}) than the modelled grid (SCR_g). As a result, the critical boundary condition associated with the loss of stability is reached seemingly at higher SCR values in RTS (SCR_g^{crt}), leading to a rightward shift of the stability boundary. In other words, to align the stability curves across platforms, the results should be referenced to the effective grid condition (SCR_{eff}) rather than the modelled grid (SCR_g). With this hypothesis, the effective critical

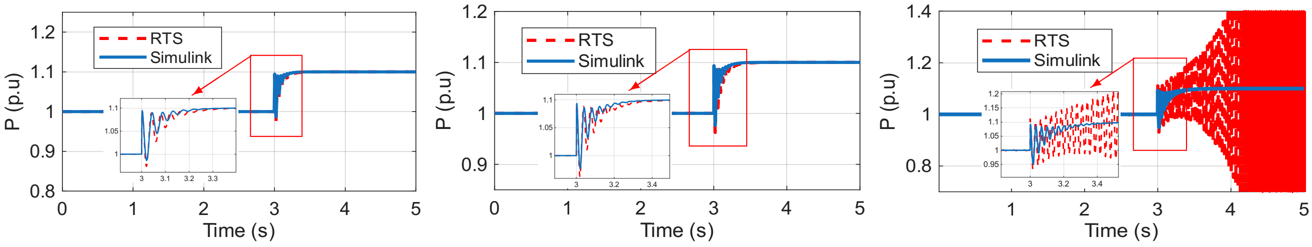

(a) SCR=6 (b) SCR=5 (c) SCR=3.3

Fig. 6: Dynamic response of GFL across platforms under different SCRs.

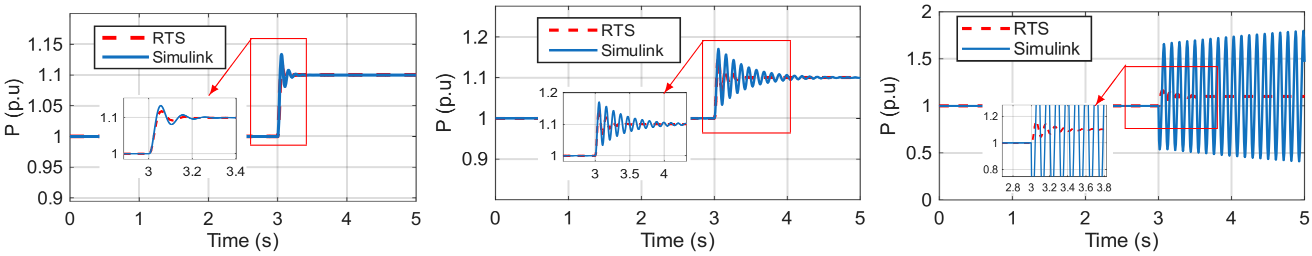

(a) SCR=4 (b) SCR=6 (c) SCR=7

Fig. 7: Dynamic response of GFM across platforms under different SCRs.

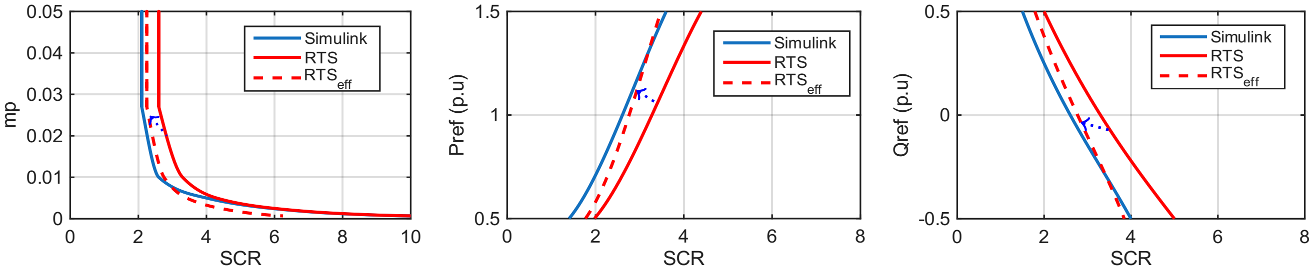

(a) m_p vs SCR (b) P_{ref} vs SCR (c) Q_{ref} vs SCR

Fig. 8: Stability boundary analysis of GFL.

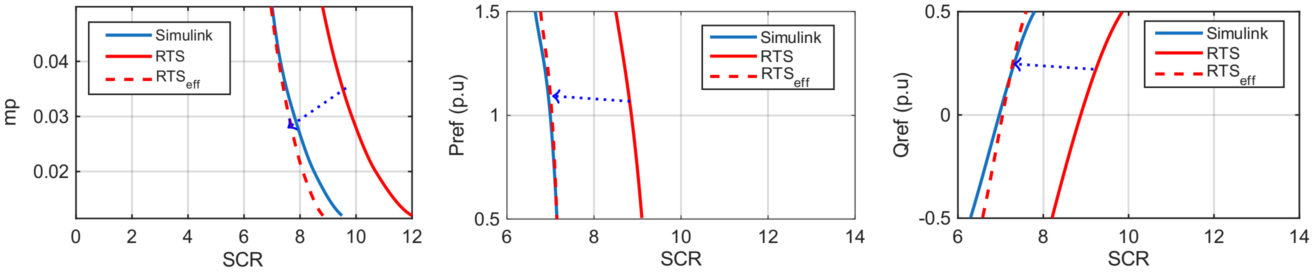

(a) m_p vs SCR (b) P_{ref} vs SCR (c) Q_{ref} vs SCR

Fig. 9: Stability boundary analysis of GFM.

grid impedance Z_{eff}^{crt} and effective critical stability boundary (SCR_{eff}^{crt}) in RTS can be calculated by using the Eq. 4 and Eq.5 that comes from Eq.2 and Eq.3.

$$Z_{\text{eff}}^{crt} = Z_g^{crt} + \boxed{Z_d} \tag{4}$$

$$\text{SCR}_{\text{eff}}^{crt} = \frac{SCR_{\text{g}}^{crt}}{1 + Z_{\text{d}} * SCR_{\text{g}}^{crt}} \tag{5}$$

By using Eq.5, the stability curves in Fig.8 and Fig.9 can be translated to lower SCR values (red dashed lines) and match the Simulink ones for Z_d=0.03pu in GFM and 0.06pu

Table 3: Δ SCR comparison for Case A and Case B

Case	mp vs SCR		Pref vs SCR		Qref vs SCR	
	Case A	Case B	Case A	Case B	Case A	Case B
GFL	0.5138	0.7665	0.6754	0.1846	0.7215	0.1841
GFM	2.0763	0.2963	1.8793	0.0458	1.9350	0.1451

Note: Case A – Simulink & RTS; Case B – Simulink & RTS$_{\text{eff}}$.

in GFL, which validates the hypothesis.

This insight can now explain the deviation in the dynamic responses across platforms observed in Fig.6 and Fig.7. By treating the grid always weaker than it is, RTS infers instability in GFL at not-so-weak grids when it should be stable (Fig.6(c), and stability in too strong grids when it shouldn't (Fig.7(c). The difference in SCR_{crt} ($\varDelta$ SCR) has been calculated using RMSE and is presented in Table 3 for Simulink with RTS and Simulink with RTS_{eff}, highlighting the $\varDelta$ SCR without Z_d (Case A) and with Z_d (Case B). With proper modelling of Z_d and Eq.5, the stability boundaries in RTS can be translated to Simulink and vice versa. Z_d has been treated as constant in the GFL and GFM experiments (two different values for the two systems), but the evidence indicates that it varies depending on Z_g. The modelling of Z_d with the solver/platform configuration and other circuit/control elements will be explored in future work, including its potential variation across different RTS platforms. While modelling of Z_d is relatively straightforward to represent when modeling IBRs and the grid, incorporating it accurately can be more challenging in other modeling frameworks.

4 Conclusions

This work presents a systematic analysis of how platform-dependent behaviour leads to discrepancies in the dynamic response and stability representation of identical GFL and GFM inverter models. Time-domain simulations and stability boundary analyses conducted on both platforms reveal that the inverter model in RTS perceives the grid as relatively weaker than the nominal SCR indicates, due to an additive impedance (Z_d) introduced by RTS. This platform-induced impedance affects the dynamic behaviour of GFL and GFM control differently. In the case of GFL operation, the weaker perceived grid in RTS results in reduced damping, causing the system to reach instability at higher SCR values. In contrast, under GFM operation, the relatively weak grid perception improves damping, thereby shifting the stability boundary to even higher SCR values.

Overall, this RTS-specific behaviour leads to a systematic horizontal shift in the stability boundaries for both GFL and GFM control modes. By explicitly accounting for Z_d, the proposed mathematical framework successfully translates stability boundaries obtained on one platform to the other, demonstrating good agreement and validating the approach.

Acknowledgments This work has been conducted within the UNIFORM project and supported by UKRI under the Grant agreement EP/Y001575/1.

References

1. F. Blaabjerg, R. Teodorescu, M. Liserre, and A. V. Timbus, "Overview of control and grid synchronization for distributed power generation systems," pp. 1398–1409, 10 2006.
2. X. Wang, M. G. Taul, H. Wu, Y. Liao, F. Blaabjerg, and L. Harnefors, "Grid-synchronization stability of converter-based resources - an overview," *IEEE Open Journal of Industry Applications*, vol. 1, pp. 115–134, 2020.
3. X. Gao, G. S. Member, D. Zhou, S. Member, A. Anvari-Moghaddam, and F. Blaabjerg, "Stability analysis of grid-following and grid-forming converters based on state-space modelling," *IEEE TRANSACTIONS ON INDUSTRY APPLICATIONS*, vol. 60. [Online]. Available: https://www.ieee.org/publications/rights/index.html
4. D. Sharma, F. Sadeque, and B. Mirafzal, "Synchronization of inverters in grid forming mode," *IEEE Access*, vol. 10, pp. 41 341–41 351, 2022. [Online]. Available: https://ieeexplore.ieee.org/document/9757217
5. M. Nurunnabi, S. Li, and H. S. Das, "Advancing grid-forming inverter technology: Comprehensive pq capability and performance analysis," *IEEE Access*, vol. 13, pp. 73 391–73 407, 2025.
6. M. Wang, Y. Zhang, A. D. Ahmed, and K. Meng, "Dynamic response of grid-following and grid-forming inverters when encountering disturbances," in *2023 IEEE International Conference on Energy Technologies for Future Grids, ETFG 2023*. Institute of Electrical and Electronics Engineers Inc., 2023.
7. N. Guruwacharya, S. Chakraborty, G. Saraswat, R. Bryce, T. M. Hansen, and R. Tonkoski, "Data-driven modeling of grid-forming inverter dynamics using power hardware-in-the-loop experimentation," *IEEE Access*, vol. 12, pp. 52 267–52 281, 2024.
8. X. Gao, D. Zhou, A. Anvari-Moghaddam, and F. Blaabjerg, "Seamless switching method between grid-following and grid-forming control for renewable energy conversion systems," *IEEE Transactions on Industry Applications*, vol. 61, no. 1, pp. 597–606, 2025.
9. Y. Pavankumar, X. Luo, E. Batzelis, A. Singh, G. Saridaki, P. Kotsampopoulos, and N. Hatziargyriou, "Seamless transition between grid forming and grid following inverters based on online grid impedance estimation." IEEE Power Energy Society General Meeting (PESGM), 11 2025, pp. 1–5.
10. C. Yu, Q. Wang, W. Fang, Y. Wang, H. Diao, H. Xu, and L. Guo, "Research on dynamic and steady-state characteristics of grid-following/grid-forming hybrid control based on model predictive control," *IEEE Open Journal of Power Electronics*, vol. 6, pp. 909–918, 2025.
11. F. Han, X. Zhang, M. Li, F. Li, and W. Zhao, "Stability control for grid-connected inverters based on hybrid-mode of grid-following and grid-forming," *IEEE Transactions on Industrial Electronics*, vol. 71, pp. 10 750–10 760, 9 2024.
12. X. Luo, E. Batzelis, A. Singh, G. Saridaki, and P. Kotsampopoulos, "Stability boundary analysis of grid-forming and grid-following inverters," in *IET Conference Proceedings*, vol. 2024. Institution of Engineering and Technology, 2024, pp. 245–250.
13. W. Ren, M. Sloderbeck, M. Steurer, V. Dinavahi, T. Noda, S. Filizadeh, A. R. Chevrefils, M. Matar, R. Iravani, C. Dufour, J. Belanger, M. O. Faruque, K. Strunz, and J. A. Martinez, "Interfacing issues in real-time digital simulators," *IEEE Transactions on Power Delivery*, vol. 26, pp. 1221–1230, 4 2011.
14. P. C. Kotsampopoulos, F. Lehfuss, G. F. Lauss, B. Bletterie, and N. D. Hatziargyriou, "The limitations of digital simulation and the advantages of phil testing in studying distributed generation provision of ancillary services," *IEEE Transactions on Industrial Electronics*, vol. 62, pp. 5502–5515, 9 2015.
15. R. Salcedo, E. Corbett, Smith *et al.*, "Banshee distribution network benchmark and prototyping platform for hardware-in-the-loop integration of microgrid and device controllers," *The Journal of Engineering*, vol. 2019, no. 8, pp. 5365–5373, 2019.
16. J. Bélanger, P. Venne, and J.-N. Paquin, "The what , where and why of real-time simulation," 2010. [Online]. Available: https://api.semanticscholar.org/CorpusID:10452935